ORIGINAL RESEARCH

Highly sensitive and selective 2-nitroaniline chemical sensor based on Ce-doped SnO$_2$ nanosheets/Nafion-modified glassy carbon electrode

Ahmad Umar[1,2] · Rajesh Kumar[3] · Hassan Algadi[2,4] · Jahir Ahmed[2] · Mohammed Jalalah[2,4] · A. A. Ibrahim[1,2] · Farid A. Harraz[2] · Mabkhoot A. Alsaiari[2,5] · Hasan Albargi[2,6]

Abstract

In this paper, pure SnO$_2$ and Ce-doped SnO$_2$ nanosheets were synthesized through a facile hydrothermal method. The synthesized materials were characterized by different techniques for their physico-chemical properties. The XRD data indicated the characteristic tetragonal rutile crystal phase for SnO$_2$. Ce doping was ascertained by the presence of the diffraction peaks of CeO$_2$ in all the doped samples of the SnO$_2$ nanosheets. FESEM images revealed highly rough surfaces as well as the agglomeration of a large number of small nanoparticles of multiple shapes to form nanosheets like morphologies for pure SnO$_2$ and Ce-doped SnO$_2$. Electrochemical techniques like cyclic voltammetry (CV), electrochemical impedance spectroscopy (EIS), and chronoamperometry were applied to demonstrate the electrochemical performances of the pure SnO$_2$ and Ce-doped SnO$_2$ nanosheets/Nafion-modified glassy carbon electrode (GCE). The 3% Ce-doped SnO$_2$ nanosheet/Nafion-modified GCE showed a remarkable sensitivity of 0.9986 µA µM^{-1} cm^{-2} over a linear dynamic range of 0.5–20.3 µM. The corresponding linear regression equation was Ip (µA) = 0.0709 [2-nitroaniline (µM)] + 0.1385 with R^2 = 0.99325. The LOD of the modified sensor was found to be 6.3 ± 0.1 nM at the signal-to-noise ratio of S/N = 3. The newly developed sensor electrode exhibited good selectivity toward 2-nitroaniline in the presence of common interfering species.

Keywords Ce-doped · SnO$_2$ · Nanosheets · Electrochemical sensor · 2-Nitroaniline

1 Introduction

Tin dioxide (SnO$_2$) due to its excellent optical and electrical properties has been reported for applications such as supercapacitors [1], gas and chemical sensors [2], lithium-ion batteries [3], dye-sensitized solar cells [4], antimicrobial agents [5], electrochemical biosensors [6], and electrocatalysis [7]. A wide variety of applications associated with SnO$_2$ nanostructures are due to the ease of synthesis of SnO$_2$ nano/microstructures with versatile morphologies, n-type semiconducting nature, a wide-band gap of 3.6 eV, high carrier density, and excellent chemical and thermal stabilities [8]. However, for further improvement for specific applications, many methods have been adopted. Among the various methods adopted, doping is considered as one of the best methods for altering the microstructural, surface morphology, electronic, optical, and bandgap properties of the SnO$_2$ nano/microstructures [9].

Cerium-a lanthanide element has received extensive attention as a dopant material for semiconductor metal

✉ Ahmad Umar
  ahmadumar786@gmail.com

1. Department of Chemistry, Faculty of Science and Arts, Najran University, P.O. Box 1988, Najran 11001, Kingdom of Saudi Arabia

2. Promising Centre for Sensors and Electronic Devices (PCSED), Najran University, P.O. Box: 1988, Najran 11001, Kingdom of Saudi Arabia

3. Department of Chemistry, Jagdish Chandra DAV College Dasuya Hoshiarpur, Punjab, India

4. Department of Electrical Engineering, Faculty of Engineering, Najran University, P.O. Box 1988, Najran 11001, Kingdom of Saudi Arabia

5. Department of Chemistry, Faculty of Science and Arts, Sharurah Branch, Najran University, Sharurah, Saudi Arabia

6. Department of Physics, Faculty of Science and Arts, Najran University, P.O. Box 1988, Najran 11001, Kingdom of Saudi Arabia

oxides due to its mixed valences of +3 and +4, availability of vacant 4f orbitals, redox characteristics ($Ce^{4+} \leftrightarrow Ce^{3+}$), rapid oxygen ion mobility, and electrocatalytic properties [10–13]. The reduction of Ce^{4+} to Ce^{3+} ion has been found to initiate the generation of lattice mobile oxygen, which in turn results in the formation of surface oxygen vacancy defects. These defects act as hot spots for the synergistic binding of other nanomaterials especially the metal oxides [14, 15]. Ce-doped metal oxides such as Ce-doped ZnO nanoparticles [16, 17], Ce-doped SnO_2 thin films [18], Ce-doped NiO nanoparticles [19], Ce-doped In_2O_3 nanostructure [20], Ce-doped hierarchical flower-like In_2O_3 microspheres [21], Ce-doped Fe_3O_4 magnetic particles [22], Ce-doped NiO micro-flowers [23], Ce-doped TiO_2 nanoparticles [24], Ce-doped WO_3 with raspberry-like architecture [25], Ce-doped CuO nanoparticles [26], and many more have been explored and reported for a variety of applications.

Among the various applications, the electrochemical sensors based on Ce-doped semiconductor metal oxide nanomaterials have extensively been fabricated to detect hazardous and toxic chemicals. One such class of hazardous materials is of nitroanilines which are the derivatives of aniline and exist in different isomeric forms. These chemicals are widely used as raw materials in industries such as dyes, pharmaceuticals, polymers, developing agents, gasoline, insecticides, pesticides, rubber, photo-stabilizers, antioxidants, explosives, anti-aging agents, and paints [27, 28]. Excess release of these chemicals as effluents into the water bodies has a devastating effect not only on the environment but also on human health. In living beings, these chemicals can potentially cause damage to the liver, kidneys, DNA mutations upon inhalation, and even skin diseases. As far as environmental effects are concerned, nitroanilines are non-biodegradable and hence are considered as typical organic pollutants [29]. Many metal oxide semiconductor materials have been explored as transducers for the sensing of nitro-anilines. Bitter gourd–shaped Yb_2O_3-doped ZnO nanostructures [30], ZnO nanoflower CeO_2 nanoparticles [31], ZnO nanorods on fluorine-doped SnO_2 [27], Sm_2O_3-doped ZnO beech fern hierarchical structures [32], novel sphere-like Co_2SnO_4 [33], K^+ intercalated MnO_2-rGO composite [34], Yb-doped ZnO nanopencils [35], CdO-ZnO hexagonal nanocones [36], etc. have been reported as electrochemical sensor materials towards nitroaniline isomers. Since Ce-doped SnO_2 nanomaterials show improved electric and electronic properties as compared to pure SnO_2, they can be potential materials for electrochemical sensing applications. Further, limited studies have been conducted to use Ce-doped SnO_2 nanomaterials for 2-nitroaniline detection.

Therefore, the main focus of the present research conducted herein was to synthesize pure SnO_2 and Ce-doped SnO_2 nanosheets with different Ce- concentrations through a facile hydrothermal method. As-synthesized materials were characterized through different techniques to confirm the composition, morphology, crystallinity, and optical and vibrational properties. The electrochemical sensing behavior of Ce-doped SnO_2 nanosheets was compared with that of pure SnO_2 nanosheets for 2-nitroaniline. It was found that the 3% Ce-doped SnO_2 nanosheets/Nafion-modified GCE exhibited.

2 Experimental details

2.1 Materials

To synthesize Ce-doped SnO_2 nanosheets, all chemicals of AR grade were procured from Sigma-Aldrich and used as obtained without any further purification. For the synthesis, various chemicals, i.e., stannous chloride dihydrate [$SnCl_2 \cdot 2H_2O$], cerium(III) chloride heptahydrate [$CeCl_3 \cdot 7H_2O$], hexamethylenetetramine [HMTA; $C_6H_{12}N_4$], and ammonium hydroxide [NH_4OH], were used. For the sensing purpose, 2-nitroaniline (2-NA) was also procured from Sigma-Aldrich and used as obtained. To prepare all solutions for the synthesis and sensing applications, deionized (DI) water was used.

2.2 Synthesis of pure SnO_2 and Ce-doped SnO_2 nanosheets

A facile hydrothermal process was used to synthesize pure and Ce-doped SnO_2 nanosheets. For the synthesis of SnO_2 nanosheets, 100 mM equimolar aqueous solutions of $SnCl_2 \cdot 2H_2O$ and HMTA (40 mL each) were mixed well under stirring for 30 min. Consequently, several drops of NH_4OH were added, to maintain the solution pH = 11, into the resultant mixture and stirred again for further 30 min. After vigorous stirring, the obtained solution was transferred to a Teflon-lined stainless steel autoclave which was sealed and heated at 160 °C for 8 h. After the desired reaction time, the autoclave was cooled to room temperature and the obtained precipitate was centrifuged and washed several times with DI water and ethanol. Finally, the obtained white precipitate was dried at room temperature and annealed at 450 °C for 3 h.

Ce-doped SnO_2 nanosheets were prepared following the same synthetic procedure of SnO_2 nanosheets; however, for Ce doping, different concentrations of $CeCl_3 \cdot 7H_2O$ (1 mM for 1%, 3 mM for 3% and 5 mM for 5%), made in 20 mL DI water, were added in the mixture of $SnCl_2 \cdot 2H_2O$ and HMTA, then completed the same hydrothermal procedure of SnO_2 nanosheets as described above.

2.3 Characterizations

The synthesized pure SnO_2 and Ce-doped SnO_2 materials were analyzed by several techniques to examine the morphologies, crystal structures and phases, composition, and optical and vibrational properties. Morphology, composition, purity, and elemental distribution in the material matrix were analyzed through field-emission scanning electron microscopy (FESEM: JEOL-JSM-7600F, Hitachi, Japan) attached with EDS for elemental mapping and composition. The crystallinity, crystal size, and crystal phases were determined by X-ray diffractometer (XRD; PANalyticalX'Pert PRO; Cu-Kα radiations source with $\lambda = 0.1542$ nm) in the range of 20–80° with a scan speed of 2°/min. Bandgap energies were determined by UV–vis spectroscopy (Perkin Elmer-UV/VIS, Lambda 950). Vibrational properties were examined by FTIR spectroscopy (Perkin Elmer-FTIR Spectrum-100). FTIR analysis of the synthesized nanomaterials was carried out by initially mixing the product homogeneously with powdered KBr (1% by weight of the sample) followed by palletization at high pressure. The scattering properties of the synthesized nanomaterials were investigated by Raman scattering (Perkin Elmer-Raman Station-400 series) at room temperature. Raman analysis was carried out by directly placing the dry powders of the synthesized nanomaterials below the probe.

2.4 Fabrication of 2-nitroaniline chemical sensors

Initially, the glassy carbon electrode (GCE) with apparent surface area 0.071 cm^2 (BAS Inc. Japan) was thoroughly polished with a 1-µm polishing diamond followed by polishing with 0.05 µm alumina slurry. After that, the polished electrode was washed several times with distilled water and dried in an air oven at 100 °C for 1 h. The surface of the GCE was coated with a thin layer of hydrothermally synthesized sensor materials. A homogeneous suspension from the sensor materials was made using Nafion solution as a conducting binder to provide stability and firmness to the coated material on the surface of the electrode. Typically, 5.0 mg of active material was dispersed in 0.45 mL of propan-2-ol containing 0.05 mL of 5% Nafion, followed by ultra-sonication for 20 min to get a homogeneous suspension. Of this suspension, 1.5 µl was gently coated onto a clean GCE surface and dried at ambient conditions for 5 min, followed by drying at 60 °C for 20 min to get a homogeneous layer of active material on the GCE surface. A three-electrode electrochemical cell connected to an electrochemical workstation (Zahner Zennium, Germany) was used for various electro-analytical measurements. A Pt wire as a counter electrode, modified GCE as a working electrode, and an Ag/AgCl (saturated KCl) electrode as a reference electrode were used. All the electro-analytical observations were recorded in 0.1 M phosphate-buffered solution (PBS) of pH 7.0 at room temperature. The sensitivity of the fabricated sensor was determined from the slope of the calibration curve divided by the active area of the modified electrode.

3 Results and discussion

3.1 Properties of the pure SnO_2 and Ce-doped SnO_2 nanosheets

The diffraction peaks of the SnO_2 lattice planes are shown in the form of an XRD spectrum in Fig. 1. Well-defined diffraction peaks corresponding to (110), (101), (200), (111), (211), (220), (002), (310), (112), (301), (202), and (321) diffraction planes are well-matched with the reported literature [37–39] and JCPDS: 41–1445. The XRD data indicated the characteristic tetragonal rutile crystal phase of SnO_2. The presence of CeO_2 in all the prepared doped samples of the SnO_2 nanosheets is confirmed by the presence of a small but well-defined peak corresponding to (111) diffraction plane which indicated the cubic fluorite phase of CeO_2(JCPDS card no. 81–0792) [40, 41]. No other peak was detected, except for SnO_2 and CeO_2 in the XRD spectra of un-doped and doped samples which further confirmed the high purity of the samples. The crystallite size was calculated using the *Scherrer* equation (Eq. 1) [42, 43].

$$d = \frac{0.89\lambda}{\beta cos\theta} \tag{1}$$

Here, λ = wavelength of X-rays (1.542 Å), β = full width half maximum (FWHM), and θ = Bragg angle of diffraction.
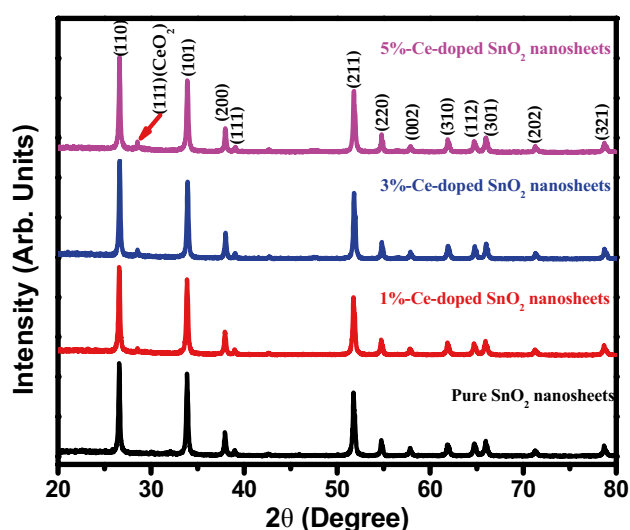

**Fig. 1** XRD spectra of the pure SnO_2, 1%, 3%, and 5% Ce-doped SnO_2 nanosheets

For analysis, the three most intense peaks corresponding to (110), (101), and (211) diffraction planes were considered. The resulting parameters are tabulated in Table 1. The average crystallite sizes for pure SnO_2, 1%, 3%, and 5% Ce-doped SnO_2 nanosheets were found to be 31.07, 30.19, 32.10, and 33.86 nm, respectively. Nominal change in the diffraction angles for Ce-doped SnO_2 nanosheets as compared to pure SnO_2 further confirmed the replacement of the Sn^{4+} ions by Ce^{4+} ions from some of the lattice points from the tetragonal rutile crystal phase of SnO_2. However, for pure SnO_2 and 1% Ce-doped SnO_2 nanosheet diffraction angles were almost the same due to the very low concentration of the dopant. With the increase in dopant concentration diffraction angles were found to increase.

The FESEM images of the pure SnO_2 and Ce-doped SnO_2 nanosheets are shown in Fig. 2a–p. Panoramic images reveal highly rough surfaces and illustrate that the pure, as well as Ce-doped SnO_2 nanosheets, are formed by the agglomeration of a large number of small nanoparticles of multiple shapes. High-resolution FESEM images showed that the thickness of the 3% Ce-doped SnO_2 nanosheets (Fig. 2j–l) was more as compared to 5% Ce-doped SnO_2 nanosheets (Fig. 2n–p). The cross-edge sections FESEM image of pure SnO_2 and Ce-doped SnO_2 nanosheets displayed a dense distribution and close packing of the nanoparticles to form layered nanosheets. For 3% Ce-doped SnO_2 nanosheets, a comb-like morphology was also observed from cross-edged FESEM images. Such small nanoparticle-layered nanosheets of pure SnO_2 and Ce-doped SnO_2 provide a large surface area for the chemisorption of analytes, required as an important pre-requisite to perform the role of electron mediator, by synthesized nanosheets for efficient and reliable electrochemical sensing.

EDS-selected area and the corresponding EDS spectrum of pure SnO_2 are shown in Fig. 3a and (a₁), respectively. The EDS

spectrum showed peaks for Sn and O only. The EDS spectrum without any other peaks corresponding to any impurities confirms the fact that the synthesized SnO_2 nanosheets have appreciable purity. To further confirm the EDS results, the composition and element distribution of the constituent elements of SnO_2 nanosheets were studied by the FESEM-elemental mapping technique (Fig. 3 (a₂, a₃)). The uniform distribution of Sn and O content in the entire structure of the nanosheets lattice can be seen. Similar to pure SnO_2 nanosheets, the Ce-doped SnO_2 nanosheets were also analyzed by EDS selected area, EDS spectra, and FESEM-elemental mapping technique. The doping of the Ce^{4+} into the crystal lattices of the SnO_2 nanosheets was confirmed for all the doped samples. The EDS spectra for all the doped nanosheets exhibited peaks for Sn, O, and Ce only. The fact was further supported by the FESEM-elemental mapping images as portrayed in Fig. 3 (b₂–b₄) for 1% Ce-doped, Fig. 3 (c₂–c₄) for 3% Ce-doped and Fig. 3 (d₂–d₄) for 5% Ce-doped SnO_2 nanosheets. The Sn, Ce, and O contents were uniformly distributed in doped SnO_2 nanosheets.

The molar ratio of $[Sn^{2+}]$ and $[OH^-]$, pH of the growth solution, and the presence of directing agents like HMTA significantly affect the shape, size, and aspect ratio of the SnO_2 nanomaterials [44]. NH_4OH present in the reaction mixture provides a sufficient amount of HO^- ions which control the nucleation and crystal growth process which then controls the shape, size, and morphology of the SnO_2 nanostructures. The presence of the HMTA further adds to the concentration of HO^- ions by hydrolysis (Eqs. 2 and 3).

$$(CH_2)_6N_4 + 6H_2O \rightarrow 6\ HCHO + 4NH_3 \tag{2}$$

$$NH_4OH \rightarrow NH_4^+ + HO^- \tag{3}$$
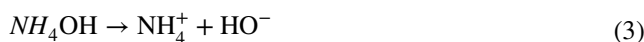
During the hydrothermal growth at 160 °C for 8 h, initially, there is the formation of different hydroxylated species like

Table 1 Various XRD parameters for pure SnO_2 and different Ce-doped SnO_2 nanosheets

Sensor	Diffraction planes	Diffraction angles (°)	FWHM (β)	Crystallite size (nm)	Average crystallite size (nm)
Pure SnO_2	(110)	26.57	0.23571	34.27	31.07
	(101)	33.88	0.26106	31.48	
	(211)	51.79	0.31835	27.45	
1% Ce- doped SnO_2	(110)	26.57	0.25033	32.27	30.19
	(101)	33.87	0.26335	31.21	
	(211)	51.79	0.32264	27.09	
3% Ce- doped SnO_2	(110)	26.61	0.2324	34.76	32.10
	(101)	33.91	0.25423	32.33	
	(211)	51.82	0.29918	29.22	
5% Ce- doped SnO_2	(110)	26.62	0.22554	35.82	33.86
	(101)	33.93	0.23432	35.08	
	(211)	51.84	0.28507	30.67	
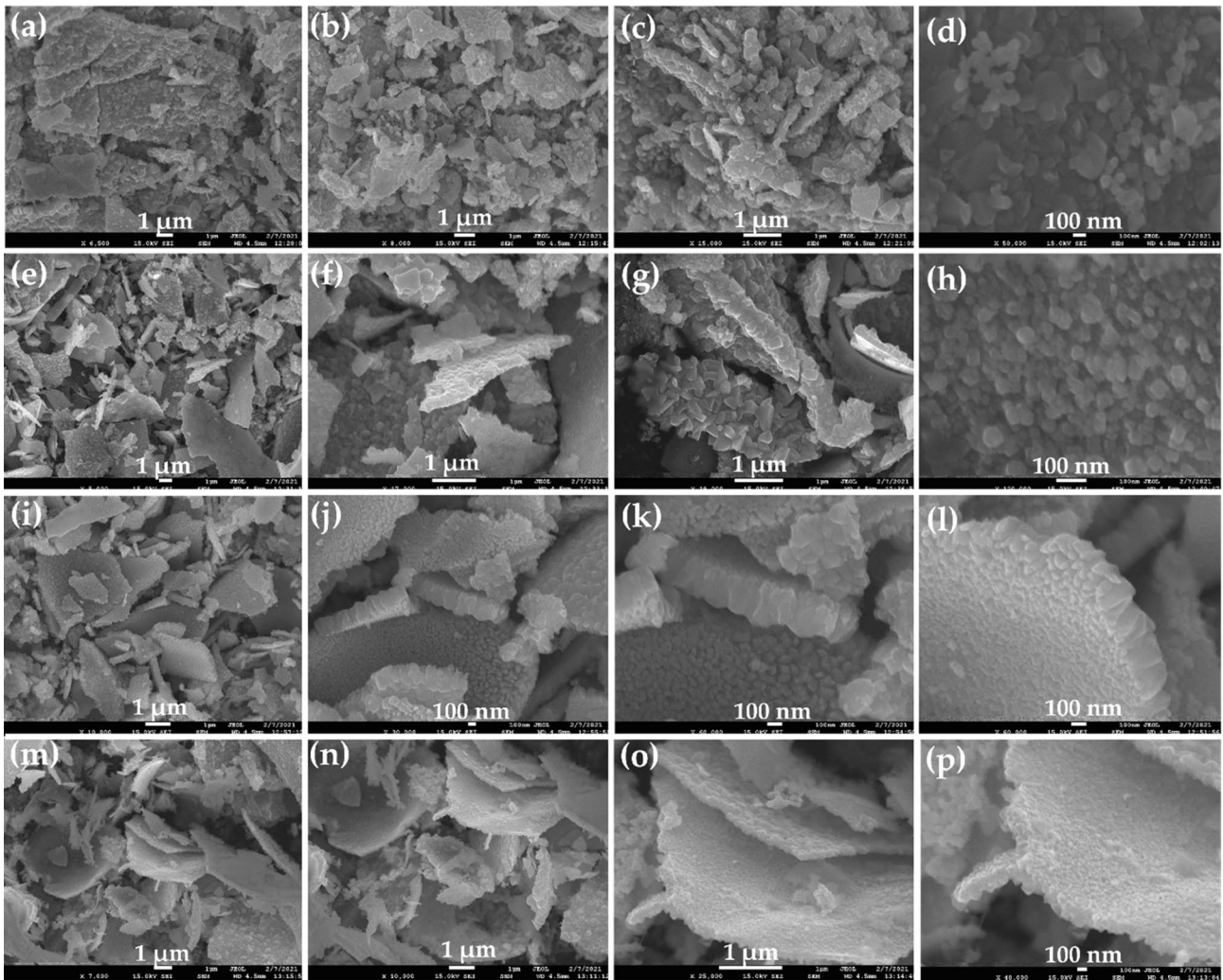
Fig. 2 FESEM images for (**a–d**) pure SnO_2, (**e–h**) 1% Ce-doped SnO_2, (**i–l**) 3% Ce-doped SnO_2, and (**m–p**) 5% Ce-doped SnO_2 nanosheets

$Sn(OH)_3^-$, $Sn(OH)_4^{2-}$, and $Sn(OH)_2$ in alkaline medium with pH 11 (Eqs. 4–6) [45, 46].

$$Sn^{2+} + 3HO^- \rightarrow Sn(OH)_3^- \tag{4}$$

$$Sn^{2+} + 4HO^- \rightarrow Sn(OH)_4^{2-} \tag{5}$$

$$Sn^{2+} + 2HO^- \rightarrow Sn(OH)_2 \tag{6}$$

During the nucleation, these hydroxides are converted to SnO at high growth temperature and pressure conditions in the autoclave. High-temperature annealing in the presence of air at 450 °C for 3 h oxidizes SnO to SnO_2 nanoparticles which aggregate together to result in the formation of layered nanosheets like morphologies (Eqs. 7–9) [39].

$$Sn(OH)_3^- \rightarrow SnO + HO^- + H_2O \tag{7}$$

$$Sn(OH)_4^{2-} \rightarrow SnO + 2 HO^- + H_2O \tag{8}$$

$$2SnO + O_2 \rightarrow 2SnO_2 \tag{9}$$
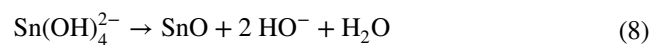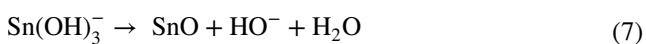
The presence of $CeCl_3 \cdot 7H_2O$, during the hydrothermal synthesis of Ce-doped SnO_2 nanosheets, results in the formation of $Ce(OH)_3$ and $Ce(OH)_4^-$ in strong alkaline medium (Eqs. 10, 11). Due to electrostatic interactions, $Ce(OH)_3$ and $Ce(OH)_4^-$ are mixed easily with $Sn(OH)_3^-$, $Sn(OH)_4^{2-}$, and $Sn(OH)_2$ in the alkaline medium during the nucleation and growth process. High-temperature annealing in the presence of air oxidizes $Ce(OH)_3$ and $Ce(OH)_4^-$ hydroxides into CeO_2 (Eqs. 12,13).
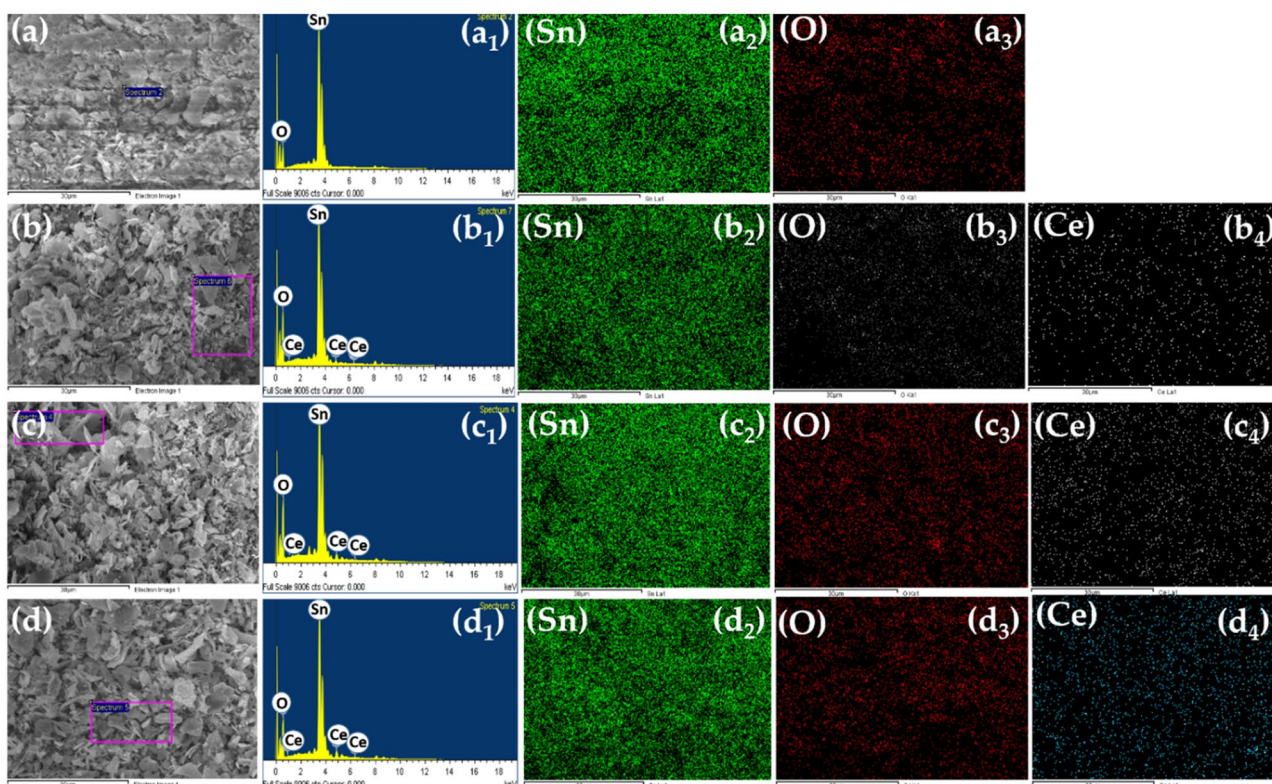
$$Ce^{3+} + 3HO^- \rightarrow Ce(OH)_3 \tag{10}$$

$$Ce^{3+} + 4HO^- \rightarrow Ce(OH)_4^- \tag{11}$$

Fig. 3 EDS selected area, EDS spectra, and FESEM-elemental mapping images for (**a**, a$_3$) pure SnO$_2$, (**b**, b$_3$) 1% Ce-doped SnO$_2$, (**c**, c$_3$) 3% Ce-doped SnO$_2$, and (**d**, d$_3$) 5% Ce-doped SnO$_2$ nanosheets

$$2\,Ce(OH)_3 + \frac{1}{2}O_2 \rightarrow 2\,CeO_2 + 3H_2O \qquad (12)$$

$$2\,Ce(OH)_4^- + \frac{1}{2}O_2 \rightarrow 2\,CeO_2 + 2\,HO^- + 3\,H_2O \qquad (13)$$
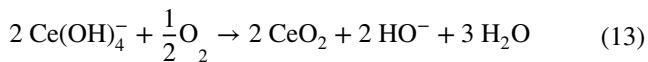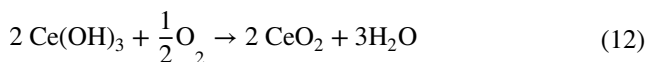
Figure 4a represents the FTIR spectra of as-synthesized pure SnO$_2$ and Ce-doped SnO$_2$ nanosheets. The fingerprint region of pure as well as Ce-doped SnO$_2$ nanosheets showed vibrational peaks in the region 604–614 cm^{-1} which may be assigned to the vibration of constituent ionic species in the crystal lattices and are due to the M − O stretching vibrations [47]. A large intensity band near 3430 cm^{-1} may be attributed to the stretching vibrational mode of O–H bonds of the H$_2$O molecules adsorbed on the surface of pure SnO$_2$ and Ce-doped SnO$_2$ nanosheets during sample preparation.

Figure 4b shows the Raman spectra of the pure SnO$_2$ and Ce-doped SnO$_2$ nanosheets. The rutile phase crystal structure of SnO$_2$ consists of two SnO$_2$ formula units per unit cell. In a single unit cell, each Sn atom is surrounded by six O-atoms whereas each O-atom is surrounded by three Sn-atoms. Symmetry point group and space group of the rutile phase of SnO$_2$ are D$_{4h}$ and p42/mnm, respectively, which have 15 optical phonons with symmetry symbols A$_{1g}$ + A$_{2g}$ + A$_{2u}$ + B$_{1g}$ + B$_{2g}$ + 2B$_{1u}$ + E$_g$ + 3E$_u$. Among

these, only the A$_{1g}$, B$_{1g}$, B$_{2g}$, and E$_g$ optical phonons are Raman active, and the remaining are Raman inactive [48]. The Raman spectra for the pure, as well as Ce-doped SnO$_2$ nanosheets, show three fundamental Raman-active peaks situated at 464, 630, and 766 cm^{-1}.

The peak at 464 is assigned to the vibration of oxygen and corresponds to E$_g$ Raman active mode. Peaks centered at 630 and 766 cm^{-1} are assigned to the expansion and contraction vibrational modes of Sn–O bonds and correspond to the A$_{1g}$ and B$_{2g}$ optical Raman active modes, respectively [49, 50]. Since the main Raman active peak corresponding to the F$_{2g}$ mode of CeO$_2$ cubic structure is ~463 cm^{-1} which is close to the E$_g$ Raman active mode of the SnO$_2$, no separate Raman active peak for CeO$_2$ in Ce-doped SnO$_2$ nanosheets was observed.

3.2 2-Nitroaniline chemical sensor applications of pure SnO$_2$ and Ce-doped SnO$_2$ nanosheets

Cyclic voltammograms (CV) were recorded and compared to analyze the electro-catalytic performance of bare GCE and modified GCE by pure SnO$_2$ and Ce-doped SnO$_2$ nanosheets/Nafion towards 10 µM 2-nitroaniline within the potential range + 0.5 to + 1.5 V at a scan rate of 50 mV/s in PBS at 7.0 pH vs. Ag/AgCl (saturated KCl) (Fig. 5a).
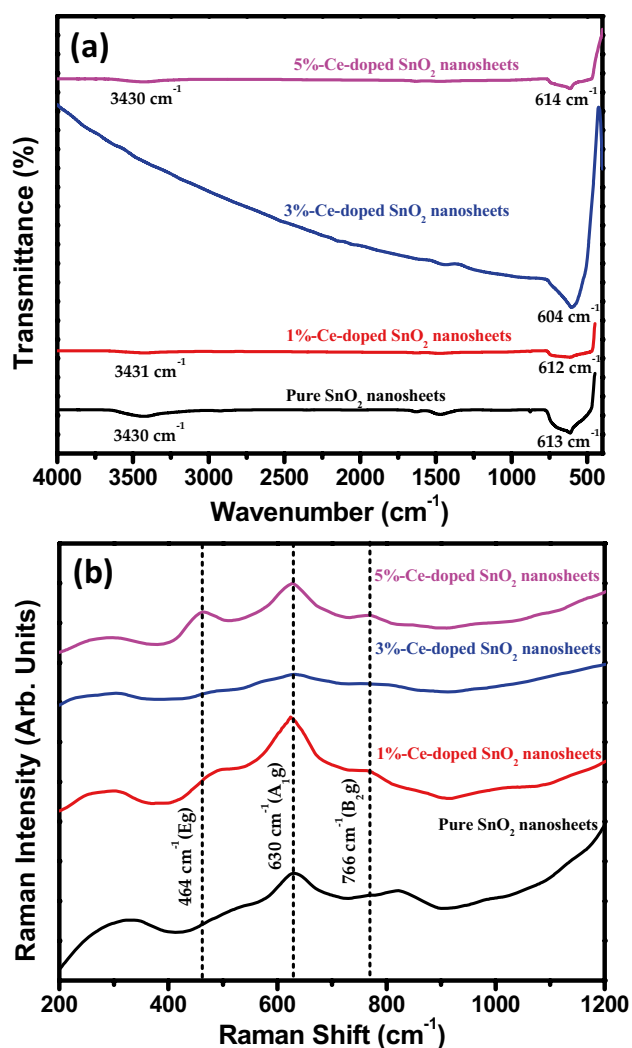
Fig. 4 (**a**) FTIR and (**b**) Raman spectra of pure SnO_2 and Ce-doped SnO_2 nanosheets

Fig. 5 (**a**) CV representing the electro-catalytic performance of bare GCE and modified GCE/Nafion electrodes based on pure SnO_2 and Ce-doped SnO_2 nanosheets towards 10 μM 2-nitroaniline within the potential range + 0.5 to + 1.5 V and at a scan rate of 50 mV/s in PBS with pH 7.0 and (**b**) CV for 3% Ce-doped SnO_2 nanosheets in the absence and presence of 10 μM 2-nitroaniline

As compared to bare GCE, the pure SnO_2 and Ce-doped SnO_2 nanosheets/Nafion modified GCE showed better electrocatalytic performances as shown by distinct anodic peaks in different voltammograms. The well-shaped reversible 2-nitroaniline oxidation peak appeared on bare as well as different modified GCEs. For bare GCE, pure SnO_2/GCE, 1% Ce-doped SnO_2/GCE, 3% Ce-doped SnO_2/GCE, and 5% Ce-doped SnO_2/GCE oxidation peak currents of 0.6165, 1.646, 1.704, 3.057, and 2.779 μA were observed at potentials 1.291, 1.496, 1.335, 1.316, and 1.336 V, respectively for 10.0 μM 2-nitroaniline at 50 mV/s in PBS. The Ce-doping into the crystal lattice of the SnO_2 nanosheets affects the microstructures, optical band gap energies, electrochemical, and redox properties of the Ce-doped SnO_2 nanosheets. Further, the unique two-dimensional sheet-like morphology, comprising very small nanoparticles, of the synthesized Ce-dope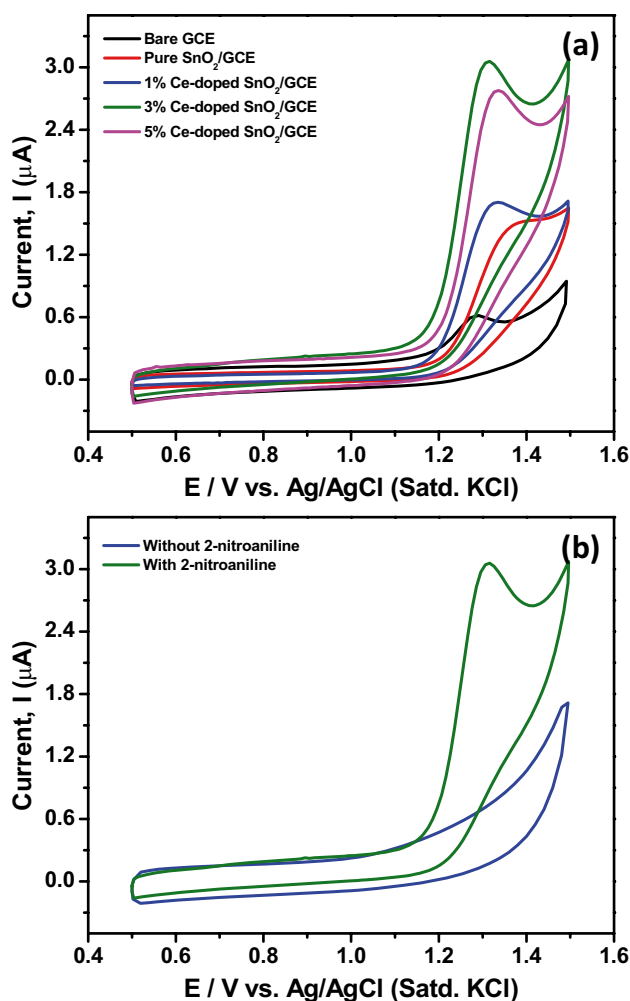d SnO_2 nanomaterials provides a large surface to volume ratio for the greater extent of adsorption of analyte species onto the surface.

Among all the modified GCEs, the electrode comprising 3% Ce-doped SnO_2 nanosheets exhibited maximum electrocatalytic activity for 10 μM 2-nitroaniline. This can be attributed to the presence of comb-like nanoparticles in case of 3% Ce-doped SnO_2 nanosheets. Therefore, in the subsequent electrochemical analysis, only 3% Ce-doped SnO_2 nanosheet/Nafion-modified GCE was studied under different conditions. This 3% Ce-doped SnO_2 nanosheet/Nafion-modified GCE showed no distinct anodic peaks in the absence of 2-nitroaniline, whereas, in the presence of 10 μM 2-nitroaniline, amplified anodic current was observed at the modified active GCE at a scan rate of 50 mV/s in PBS (Fig. 5b). Thus, as fabricated 3% Ce-doped SnO_2 nanosheet/

Nafion-modified GCE can potentially be used for electro-catalytic oxidation/reduction and hence as electrochemical sensor towards 2-nitroaniline even at very low concentration of 10 μM.

The electro-catalytic sensing characterizations of the 3% Ce-doped SnO_2 nanosheet/Nafion-modified GCE were analyzed as a function of scan rate through CV within the potential range + 0.5 to + 1.5 V. Figure 6a represents the effect of change of scan rates from 10 to 60 mV/s on the electrochemical behavior toward 5.0 μM 2-nitroaniline. With the increase in the scan rate, a continuous increase in anodic peak current was observed. A high determinant coefficient (R^2) value of 0.9643 was observed from a linearized variation of anodic peak currents with scan rates which further indicate the diffusion-controlled electrochemical oxidation

of 2-nitroaniline [51] (Fig. 6b). The corresponding calibration plot for the anodic current responses for 5.0 μM 2-nitroaniline vs. (scan rate)$^{1/2}$ with the determinant coefficient $R^2 = 0.99344$ (Fig. 6c) and the plot representing the Ep vs. log scan rate with the determinant coefficient $R^2 = 0.99801$ (Fig. 6d) for 3% Ce-doped SnO_2 nanosheets/Nafion modified GCEs were also linear confirming the pure diffusion-controlled process.

To further investigate the electrochemical properties of the pure SnO_2 and Ce-doped SnO_2 nanosheets/ Nafion-modified GCE, a comparative study of EIS was also carried out. The EIS data was collected in 1.0 mM $K_3Fe(CN)_6$/$K_4Fe(CN)_6$/0.1 M KCl solution at + 0.6 V. The AC signal amplitude was 10 mV and the frequency range was 0.1 Hz to 100 kHz. The corresponding Nyquist plots drawn between real variables (Z_{Real}) and the negative value
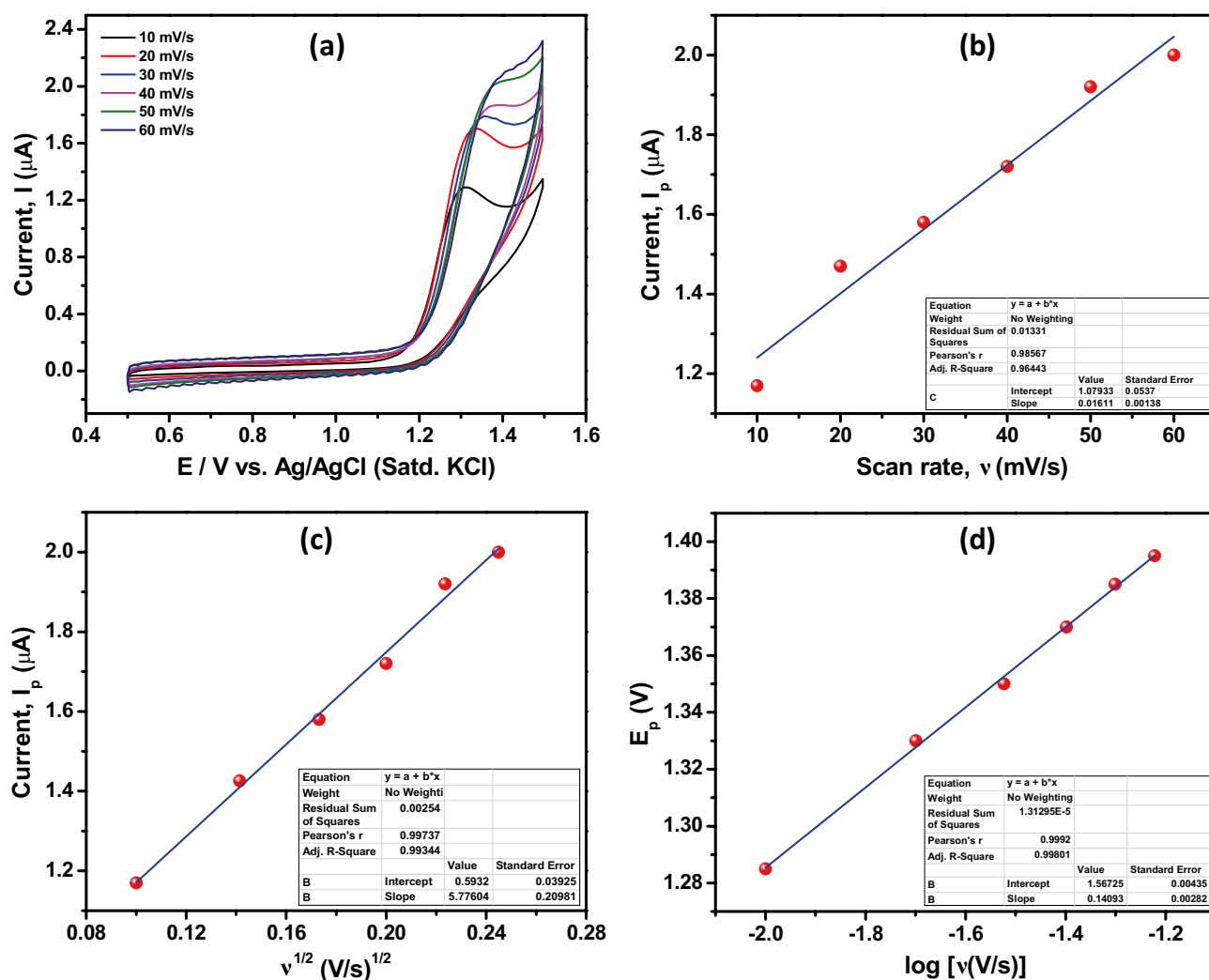

Fig. 6 (**a**) The effect of different scan rates on the CV response for 5.0 μM 2-nitroaniline, (**b**) linear plot of scan rate vs. anodic current response, (**c**) linear plot for (scan rate)$^{1/2}$ vs. anodic current response, and (**d**) log scan rate vs. Ep using 3% Ce-doped SnO_2 nanosheet/ Nafion-modified GCE
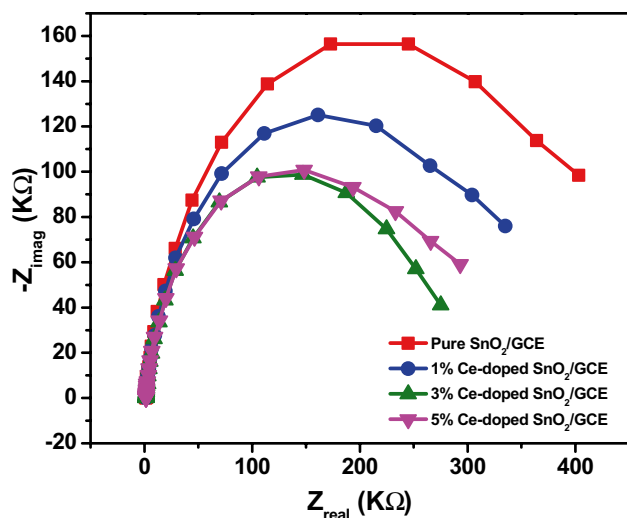
Fig. 7 Nyquist plots between Z_{Real} and $-Z_{Imag}$ for different modified electrodes

Fig. 8 (**a**) The amperometric response curve of 3% Ce-doped SnO$_2$ nanosheets/Nafion-modified GCE in the presence of different 2-nitroaniline concentrations ranging from 0.5 to 38.0 μM at an applied potential of 1.3 V in PBS and (**b**) corresponding calibration plot of [2-nitroaniline] vs. amperometric current responses

of the imaginary impedance variable (Z_{Imag}) are shown in Fig. 7. The semicircle shape of the Nyquist plots for the modified electrodes represents the electron transfer resistance, which resulted due to the electron transfer by the redox probe $[Fe(CN)_6]^{3-/4-}$. The diameter of the semicircle plot is correlated to the charge-transfer resistance (R_{ct}) which controls the rate of electron transfer kinetics of the $[Fe(CN)_6]^{3-/4-}$ probe at the interface of the electrode. As revealed, the lowest semicircle's diameter was obtained for the 3% Ce-doped SnO$_2$-modified GCE, indicating a decreased R_{ct} value for this active electrode than other modified working electrodes including pure SnO$_2$/GCE, 1% Ce-doped SnO$_2$/GCE, or 5% Ce-doped SnO$_2$/GCE. This again confirmed an enhanced electron-transfer capability for the 3% Ce-doped SnO$_2$ modified GCE which is advantageous for the electrochemical sensing performance toward 2-nitroaniline, consistent with the above CV results of Fig. 5a.

The amperometric technique was also explored under constant stirring conditions in PBS at an applied potential of 1.3 V against Ag/AgCl (saturated KCl). Figure 8a displays the current real-time response of 3% Ce-doped SnO$_2$ nanosheets/Nafion-modified GCE in the presence of different 2-nitroaniline concentrations ranging from 0.5 to 38.0 μM. In the absence of 2-nitroaniline, a stable background response was observed by the modified GCE. Amperometric current responses increased as soon as 2-nitroaniline with different concentrations was added to the PBS.

To determine the sensitivity, LOD, and LDR, a calibration plot of the amperometric response current vs. [2-nitroaniline] was plotted (Fig. 8b). The 3% Ce-doped SnO$_2$ nanosheet-modified/Nafion GCE showed a linear
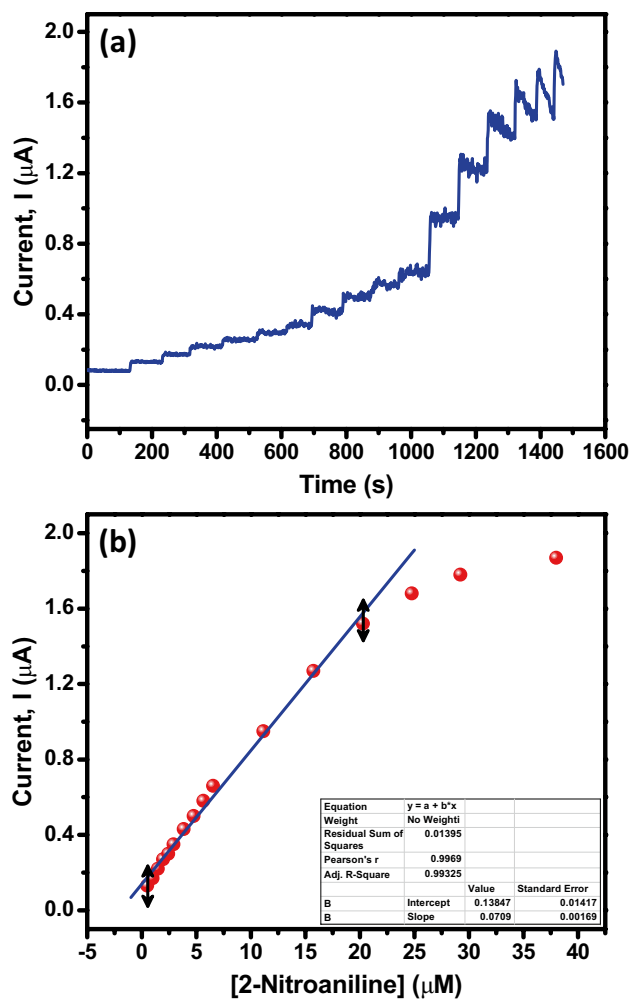
dynamic range of 0.5–20.3 μM. The corresponding linear regression equation was Ip (μA) = 0.0709[2-nitroaniline (μM)] + 0.1385 with R^2 = 0.99325. The LOD of the modified sensor was found to be 6.3 ± 0.1 nM at the signal-to-noise ratio S/N = 3. The sensitivity of the sensor is estimated to be 0.9986 μA μM^{-1} cm^{-2}.

The effect of some interfering electro-active chemical species on the selectivity of the 3% Ce-doped SnO$_2$ nanosheet/Nafion-modified GCE towards 2-nitroaniline was also examined. Figure 9 represents the variations of the amperometric current responses of modified GCE during the successive addition of 2-nitroaniline (5.0 μM), 4-nitroaniline (50 μM), 4-nitrophenol (50 μM), NaCl (50 μM), and CaCl$_2$ (50 μM) after certain time intervals and at an applied potential of 1.3 V. Significant increase in current response upon the addition of even 5.0 μM 2-nitroaniline as compared to
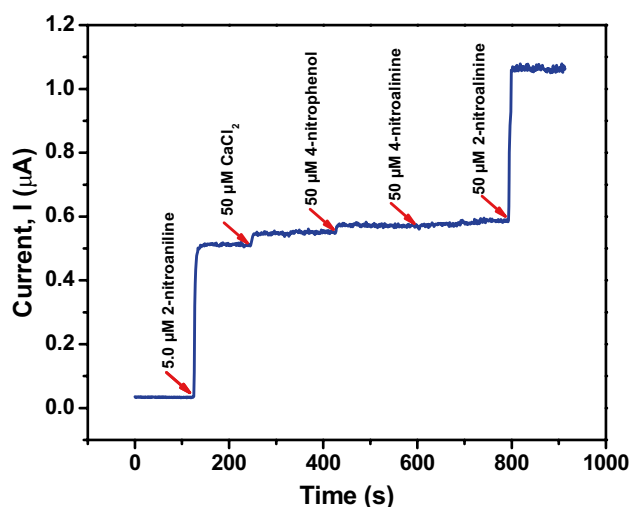
Fig. 9 Amperometric plot representing the interference behavior of different species for the electrochemical sensing of 2-nitroaniline using 3% Ce-doped SnO$_2$ nanosheets/Nafion modified GCE at 1.3 V in PBS

negligible current changes on the additions of 4-nitroaniline, 4-nitrophenol, NaCl, and CaCl$_2$, is undoubtedly confirming the excellent selectivity of the fabricated 3% Ce-doped SnO$_2$ nanosheet based sensor for 2-nitroaniline.

3.3 Sensing mechanism

Figure 10 illustrates the proposed mechanism for the better electrochemical sensing of the 2-nitroaniline by Ce-doped SnO$_2$ nanosheets. The presence of Ce^{4+} ions into the SnO$_2$ crystal lattice promotes the charge transfer from
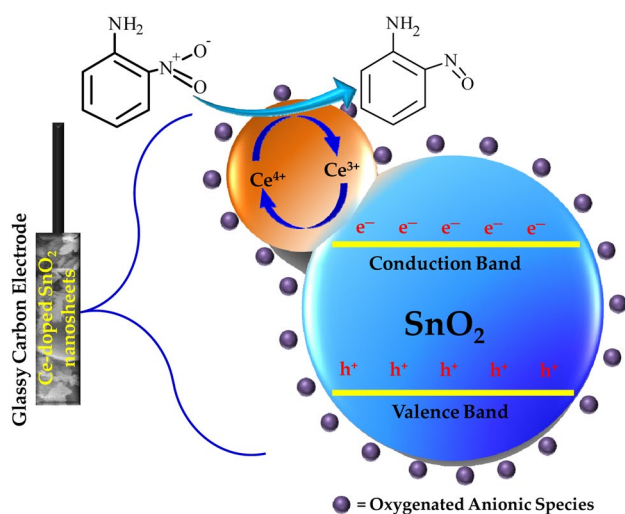
the conduction band of SnO$_2$ nanosheets to the surface-adsorbed O$_2$ molecules which were present in the PBS. Additionally, Ce-doping also increases the density of oxygen vacancies and roughness on the surface of the nanosheets required to generate sufficiently more adsorption sites for O$_2$ molecules. Conduction band electrons reduce the adsorbed O$_2$ molecules to different oxygenated species like O^-, O^{2-}, and O_2^- [30]. Further, the rates of intermolecular charge transfer process and adsorption of the 2-nitroaniline are facilitated on the surface of the Ce-doped SnO$_2$ nanosheets due to the simultaneous presence of electron-rich amino (–NH$_2$) group and an electron-deficient nitro (–NO$_2$) group [52, 53]. Different reactive oxygenated species on the surface of the nanosheets initially reduce 2-nitroaniline into 2-hydroxylamine aniline. The reduction process is followed by a fast reversible oxidation process which oxidizes the 2-hydroxylamine aniline into 2-nitrosoaniline. The electrons released during the oxidation process are transferred back to the conduction band of Ce-doped SnO$_2$ nanosheets which increases the current response and electrical conductivity [54].

Furthermore, there is significant potential for improving the sensitivity of this chemical sensor by applying external photons, which could result in improving its behavior toward 2-nitroaniline [55–57].

4 Conclusions

Herein, a novel Ce-doped SnO$_2$ nanosheet/Nafion-modified GCE has been prepared to quantify the 2-nitroaniline in PBS at pH 7.0. Among the various modified electrodes, the 3% Ce-doped SnO$_2$ nanosheets exhibited better electrochemical sensing behavior as compared to others. As-fabricated 3% Ce-doped SnO$_2$ nanosheets/Nafion-modified GCE showed a linear dynamic range of 0.5–20.3 μM, LOD 6.3 ± 0.1 nM at the signal-to-noise ratio S/N = 3 and a remarkable sensitivity of 0.9986 μA μM^{-1} cm^{-2}. High sensitivity, very low detection limit, wide dynamic range, quick response time, and excellent selectivity of the fabricated sensor may be attributed to high surface area and easy diffusion of the 2-nitroaniline into the sensor matrix. Hence, the hydrothermal synthesis of Ce-doped SnO$_2$ nanosheets has great sensor potential and can be explored for future sensing applications towards toxic and harmful chemicals.

Fig. 10 Proposed sensing mechanism for 2-nitroaniline by Ce-doped SnO$_2$ nanosheets

Declarations

Conflict of interest The authors declare no competing interests.

References

1. Xu CH, Chen JZ (2016) Atmospheric-pressure plasma jet processed SnO2/CNT nanocomposite for supercapacitor application. Ceram Int 42:14287–14291. https://doi.org/10.1016/j.ceramint.2016.06.023

2. Padvi MN, Moholkar AV, Prasad SR, Prasad NR (2021) A critical review on design and development of gas sensing materials. Engineered Science. 15. https://doi.org/10.30919/es8d431.

3. Li Y, Wang X, Wang Z, Chen L (2019) Facile synthesis of SnO2 nanorods for Na-ion batteries, ES Energy & Environment 3 (2019) 55–59. https://doi.org/10.30919/esee8c198.

4. Dimarco BN, Sampaio RN, James EM, Barr TJ, Bennett MT, Meyer GJ (2020) Efficiency Considerations for SnO2-Based Dye-Sensitized Solar Cells. ACS Appl Mater Interfaces 12:23923–23930. https://doi.org/10.1021/acsami.0c04117

5. Sumathi P (2020) Synthesis, Characterization and Antimicrobial Studies of SnO2 Nanoparticles, Int. J. Chem Tech Res. 13: 203–209. https://doi.org/10.20902/ijctr.2019.130317.

6. Yang L, Zhou Q, Wang G, Yang Y (2013) Acetylcholinesterase biosensor based on SnO2 nanoparticles-carboxylic graphene-nafion modified electrode for detection of pesticides. Biosens Bioelectron 49:25–31. https://doi.org/10.1016/j.bios.2013.04.037

7. Li X, Yan J, Zhu K (2021) Fabrication and characterization of Pt doped Ti/Sb-SnO2 electrode and its efficient electro-catalytic activity towards phenol. Engineered Science. 15 (2021). https://doi.org/10.30919/es8d432.

8. J. Divya, A. Pramothkumar, S. Joshua Gnanamuthu, D.C. Bernice Victoria, P.C. Jobe prabakar, Structural, optical, electrical and magnetic properties of Cu and Ni doped SnO2 nanoparticles prepared via Co-precipitation approach, Phys. B Condens. Matter. 588 (2020) 412169. https://doi.org/10.1016/j.physb.2020.412169.

9. Chattopadhyay S, Kumawat A, Misra KP, Halder N, Bandyopadhyay A, Antony A, Rao A, Poornesh P, Jedryka J, Ozga K, Kucharska B (2021) Micro-strain administered SHG intensity enhancement by heavy Ce doping in co-precipitated ZnO nanoparticles, Mater. Sci. Eng. B Solid-State Mater. Adv. Technol. 266:115041. https://doi.org/10.1016/j.mseb.2021.115041.

10. Chen K, Zhang H, Tong H, Wang L, Tao L, Wang K, Zhang Y, Zhou X (2021) Down-conversion Ce-doped TiO2 nanorod arrays and commercial available carbon based perovskite solar cells: Improved performance and UV photostability. Int J Hydrogen Energy 46:5677–5688. https://doi.org/10.1016/j.ijhydene.2020.11.074

11. Islam MR, Saiduzzaman M, Nishat SS, Kabir A, Farhad SFU (2021) Synthesis, characterization and visible light-responsive photocatalysis properties of Ce doped CuO nanoparticles: A combined experimental and DFT+U study Colloids Surfaces A Physicochem Eng Asp 617:126386 https://doi.org/10.1016/j.colsurfa.2021.126386

12. Kumawat A, Sharma A, Chattopadhyay S, Misra KP (2021) Temperature dependent photoluminescence in Sol-gel derived Ce doped ZnO nanoparticles. Mater Today Proc 43:2965–2969. https://doi.org/10.1016/j.matpr.2021.01.322

13. Zhang Y, Wang C, Zhao L, Liu F, Sun X, Hu X, Lu G (2021) Preparation of Ce-doped SnO2 cuboids with enhanced 2-butanone sensing performance, Sensors Actuators B Chem. 130039. https://doi.org/10.1016/j.snb.2021.130039.

14. Sawant JP, Shaikh SF, Kale RB, Pathan HM (2020)Pathan, Chemical bath deposition of CuInS2 thin films and synthesis of CuInS2 nanocrystals: A review. Engineered Science 12:1–12. https://doi.org/10.30919/es8d1142.

15. Kumar M, Chauhan MS, Akhtar MS, Umar A (2021) Effect of cerium ions in Ce-Doped ZnO nanostructures on their photocatalytic and picric acid chemical sensing. Ceram Int 47:3089–3098. https://doi.org/10.1016/j.ceramint.2020.09.145

16. Kumar R, Umar A, Kumar G, Akhtar MS, Wang Y, Kim SH (2015) Ce-doped ZnO nanoparticles for efficient photocatalytic degradation of direct red-23 dye. Ceram Int 41:7773–7782. https://doi.org/10.1016/j.ceramint.2015.02.110

17. Karunakaran C, Gomathisankar P, Manikandan G (2010) Preparation and characterization of antimicrobial Ce-doped ZnO nanoparticles for photocatalytic detoxification of cyanide. Mater Chem Phys 123:585–594. https://doi.org/10.1016/j.matchemphys.2010.05.019

18. Liang YC, Lee CM, Lo YJ (2017) Reducing gas-sensing performance of Ce-doped SnO2 thin films through a cosputtering method. RSC Adv 7:4724–4734. https://doi.org/10.1039/c6ra25853k

19. Gawali SR, Patil VL, Deonikar VG, Patil SS, Patil DR, Patil PS, Pant J (2018) Ce doped NiO nanoparticles as selective NO2 gas sensor. J Phys Chem Solids 114:28–35. https://doi.org/10.1016/j.jpcs.2017.11.005

20. Liu X, Jiang L, Jiang X, Tian X, Sun X, Wang Y, He W, Hou P, Deng X, Xu X (2018) Synthesis of Ce-doped In2O3 nanostructure for gas sensor applications. Appl Surf Sci 428:478–484. https://doi.org/10.1016/j.apsusc.2017.09.177

21. Wei D, Huang Z, Wang L, Chuai X, Zhang S, Lu G (2018) Hydrothermal synthesis of Ce-doped hierarchical flower-like In2O3 microspheres and their excellent gas-sensing properties. Sensors Actuators, B Chem 255:1211–1219. https://doi.org/10.1016/j.snb.2017.07.162

22. Qi Z, Joshi TP, Liu R, Liu H, Qu J (2017) Synthesis of Ce(III)-doped Fe3O4 magnetic particles for efficient removal of antimony from aqueous solution. J Hazard Mater 329:193–204. https://doi.org/10.1016/j.jhazmat.2017.01.007

23. Zhu L, Zeng W, Yang J, Li Y (2019) Unique hierarchical Ce-doped NiO microflowers with enhanced gas sensing performance. Mater Lett 251:61–64. https://doi.org/10.1016/j.matlet.2019.05.055

24. Dil EA, Ghaedi M, Asfaram A, Mehrabi F, Bazrafshan AA, Tayebi L (2019) Synthesis and application of Ce-doped TiO2 nanoparticles loaded on activated carbon for ultrasound-assisted adsorption of Basic Red 46 dye, Ultrason. Sonochem. 58:104702. https://doi.org/10.1016/j.ultsonch.2019.104702.

25. Diao Q, Yin Y, Jia W, Xu X, Ding Y, Zhang X, Cao J, Yang K, Jiao M (2020) Highly sensitive ethanol sensor based on Ce-doped WO3 with raspberry-like architecture Mater Res Express 7:115012 https://doi.org/10.1088/2053-1591/abcabf

26. Ponnar M, Thangamani C, Monisha P, Gomathi SS, Pushpanathan K (2018) Influence of Ce doping on CuO nanoparticles synthesized by microwave irradiation method. Appl Surf Sci 449:132–143. https://doi.org/10.1016/j.apsusc.2018.01.126

27. Aggrwal G, Salunke-Gawali S, Gejji SP, Nikalje M, Chakravarty D, Verma PL, Gosavi-Mirkute P, Harihar S, Jadhav M, Puranik VG (2021) Puranik. Reactions of 2,3-Dibromonaphthalene-1,4-Dione and Pyridyl Amines: X-ray Structures, DFT Investigations, and Selective Detection of the Hg2+ and Ni2+ Ions. Engineered Science, 14:78–93. https://doi.org/10.30919/es8d427.

28. Chen S, Chen X, Xia T, Ma Q (2016) A novel electrochemiluminescence sensor for the detection of nitroaniline based on the nitrogen-doped graphene quantum dots. Biosens Bioelectron 85:903–908. https://doi.org/10.1016/j.bios.2016.06.010

29. Nie Y, Liu Y, Su X, Ma Q (2019) Nitrogen-rich quantum dots-based fluorescence molecularly imprinted paper strip for p-nitroaniline detection. Microchem J 148:162–168. https://doi.org/10.1016/j.microc.2019.04.080

30. Umar A, Ibrahim AA, Kumar R, Almas T, Al-Assiri MS, Baskoutas S (2019) Nitroaniline chemi-sensor based on bitter gourd shaped ytterbium oxide (Yb2O3) doped zinc oxide (ZnO) nanostructures. Ceram Int 45:13825–13831. https://doi.org/10.1016/j.ceramint.2019.04.079

31. Sayyed SA, Beedri NI, Bhujbal PK, Shaikh SF, Pathan HM (2020) Pathan, Eosin Eosin-Y Sensitized Bi-layered ZnO Nanoflower-CeO2 Photoanode for Dye-Sensitized Solar Cells Application. ES Materials & Manufacturing 10:45–51. https://doi.org/10.30919/esmm5f939.

32. Ibrahim AA, Umar A, Kumar R, Kim SH, Bumajdad A, Baskoutas S (2016) Sm2O3-doped ZnO beech fern hierarchical structures for nitroaniline chemical sensor. Ceram Int 42:16505–16511. https://doi.org/10.1016/j.ceramint.2016.07.061

33. Palpandi K, Raman N (2020) Electrochemical detection of 2-nitroaniline at a novel sphere-like Co2SnO4 modified glassy carbon electrode. New J Chem 44:8454–8462. https://doi.org/10.1039/d0nj01098g

34. Yamuna A, Jiang TY, Chen SM (2021) Preparation of K+ intercalated MnO2-rGO composite for the electrochemical detection of nitroaniline in industrial wastewater J Hazard Mater 411:125054 https://doi.org/10.1016/j.jhazmat.2021.125054

35. Ahmed AI, Ahmad U, Baskoutas S (2017) Ytterbium doped zinc oxide nanopencils for chemical sensor application. J Nanosci Nanotechnol 17:9157–9162. https://doi.org/10.1166/jnn.2017.14702

36. Umar A, Akhtar MS, Al-Assiri MS, Al-Salami AE, Kim SH (2018) Composite CdO-ZnO hexagonal nanocones: Efficient materials for photovoltaic and sensing applications. Ceram Int 44:5017–5024. https://doi.org/10.1016/j.ceramint.2017.12.098

37. Umar A, Ammar HY, Kumar R, Almas T, Ibrahim AA, AlAssiri MS, Abaker M, Baskoutas S (2020) Efficient H2 gas sensor based on 2D SnO2 disks: Experimental and theoretical studies. Int J Hydrogen Energy 45:26388–26401. https://doi.org/10.1016/j.ijhydene.2019.04.269

38. Kumar R, Umar A, Kumar R, Chauhan MS, Al-Hadeethi Y (2021) ZnO–SnO2 nanocubes for fluorescence sensing and dye degradation applications. Ceram Int 47:6201–6210. https://doi.org/10.1016/j.ceramint.2020.10.198

39. Umar A, Ammar HY, Kumar R, Ibrahim AA, Al-Assiri MS (2019) Square disks-based crossed architectures of SnO2 for ethanol gas sensing applications—An experimental and theoretical investigation Sensors Actuators, B Chem 304:127352 https://doi.org/10.1016/j.snb.2019.127352

40. Umar A, Kumar R, Akhtar MS, Kumar G, Kim SH (2015) Growth and properties of well-crystalline cerium oxide (CeO2) nanoflakes for environmental and sensor applications. J Colloid Interface Sci 454:61–68. https://doi.org/10.1016/j.jcis.2015.04.055

41. Umar A, Almas T, Ibrahim AA, Kumar R, AlAssiri MS, Baskoutas S, Akhtar MS (2020) An efficient chemical sensor based on CeO2 nanoparticles for the detection of acetylacetone chemical J Electroanal Chem 864:114089 https://doi.org/10.1016/j.jelechem.2020.114089

42. Al-Hadeethi Y, Umar A, Ibrahim AA, Al-Heniti SH, Kumar R, Baskoutas S, Raffah BM (2017) Synthesis, characterization and acetone gas sensing applications of Ag-doped ZnO nanoneedles, Ceram. Int. 43:6765–6770. https://doi.org/10.1016/j.ceramint.2017.02.088.

43. Al-Hadeethi Y, Umar A, Al-Heniti SH, Kumar R, Kim SH, Zhang X, Raffah BM (2017) 2D Sn-doped ZnO ultrathin nanosheet networks for enhanced acetone gas sensing application. Ceram Int 43:2418–2423. https://doi.org/10.1016/j.ceramint.2016.11.031

44. Lupan O, Chow L, Chai G, Schulte A, Park S, Heinrich H. (2009) A rapid hydrothermal synthesis of rutile SnO2 nanowires, Mater. Sci. Eng. B. 157:101–104. https://doi.org/10.1016/j.mseb.2008.12.035.

45. Wu W, Zhang S, Zhou J, Xiao X, Ren F, Jiang C (2011) Controlled synthesis of monodisperse sub-100 nm hollow SnO2 nanospheres: A template-and surfactant-free solution-phase route, the growth mechanism, optical properties, and application as a photocatalyst. Chem - A Eur J 17:9708–9719. https://doi.org/10.1002/chem.201100694

46. Wang B, Sun L, Wang Y (2018) Template-free synthesis of nanosheets-assembled SnO2 hollow spheres for enhanced ethanol gas sensing, Mater. Lett. 218:290–294. https://doi.org/10.1016/j.matlet.2018.02.003.

47. Ray A, Roy A, Ghosh M, Ramos-Ramón JA, Saha S, Pal U, Bhattacharya SK, Das S (2019) Study on charge storage mechanism in working electrodes fabricated by sol-gel derived spinel NiMn2O4 nanoparticles for supercapacitor application, Appl. Surf. Sci. 463:513–525. https://doi.org/10.1016/j.apsusc.2018.08.259.

48. Mariammal RN, Ramachandran K, Renganathan B, Sastikumar D (2012) On the enhancement of ethanol sensing by CuO modified SnO2 nanoparticles using fiber-optic sensor. Sensors Actuators, B Chem 169:199–207. https://doi.org/10.1016/j.snb.2012.04.067

49. Poloju M, Jayababu N, Manikandan E, Reddy MR (2017) Reddy, Enhancement of the isopropanol gas sensing performance of SnO2/ZnO core/shell nanocomposites, J. Mater. Chem. C. 5:2662–2668. https://doi.org/10.1039/C6TC05095F.

50. Zargar RA, Bhat MA, Parrey IR, Arora M, Kumar J, Hafiz AK (2016) Optical properties of ZnO/SnO2 composite coated film, Opt. - Int. J. Light Electron Opt. 127:6997–7001. https://doi.org/10.1016/j.ijleo.2016.05.037.

51. Wahab R, Ahmad N, Alam M, Ahmed J (2019) Nanorods of ZnO: An effective hydrazine sensor and their chemical properties. Vacuum. https://doi.org/10.1016/j.vacuum.2019.04.036

52. Naito S, Yokoyama S, Asahara H, Nishiwaki N (2017) Synthesis of functionalized 4-nitroanilines by ring transformation of dinitropyridone with enaminones, Tetrahedron Lett. 58:4699–4702. https://doi.org/10.1016/j.tetlet.2017.11.003.

53. Muniz-Miranda M, Neto N (2004) Surface-enhanced Raman scattering of π-conjugated "push-pull" molecules: Part I. p-Nitroaniline adsorbed on silver nanoparticles, in: Colloids Surfaces A Physicochem. Eng. Asp. 79–84. https://doi.org/10.1016/j.colsurfa.2004.08.070.

54. Umar A, Akhtar MS, Dar GN, Abaker M, Al-Hajry A, Baskoutas S (2013) Visible-light-driven photocatalytic and chemical sensing properties of SnS2 nanoflakes. Talanta 114:183–190. https://doi.org/10.1016/j.talanta.2013.03.050

55. Algadi H, Mahata C, Kim S, Dalapati GK (2020) Improvement of Photoresponse Properties of Self-Powered ITO/InP Schottky Junction Photodetector by Interfacial ZnO Passivation, J. Electron. Mater. 1–7. https://doi.org/10.1007/s11664-020-08565-1.

56. Algadi H, Mahata C, Sahoo B, Kim M, Koh WG, Lee T (2020) Facile method for the preparation of high-performance photodetectors with a GQDs/perovskite bilayer heterostructure, Org. Electron. 76. https://doi.org/10.1016/j.orgel.2019.105444.

57. Algadi H, Mahata C, Woo J, Lee M, Kim M, Lee T (2019) Enhanced photoresponsivity of all-inorganic (Cspbbr3) perovskite nanosheets photodetector with carbon nanodots (CDs), Electron. 8. https://doi.org/10.3390/electronics8060678.